





Cite this: *RSC Adv.*, 2022, 12, 36063

The synergism between self-activated and impurity-related emissions of $\text{LiCa}_3\text{ZnV}_3\text{O}_{12}$: lattice distortion, energy transfer and temperature sensing effect†

Jie Li, Ruixia Shi,  Yongqiang Cao, Qian Ma,  Ling Chen,  Aiyu Zhang * and Ping Yang *

Some of the metal vanadates have special self-activated luminescence. In order to further enrich its luminous color, luminescent impurity ions can be introduced into its lattice. The interaction between the self-activated emission and the impurity-related emission remains to be studied. In this work, the synergism between the two kinds of emission in $\text{LiCa}_3\text{ZnV}_3\text{O}_{12}$ was explored from these three aspects: lattice distortion, energy transfer and temperature effect. Eu^{3+} ions replace Ca^{2+} ions in the lattice of $\text{LiCa}_3\text{ZnV}_3\text{O}_{12}$, leading to a lattice contraction of the LCZV host, which depresses the self-activating emission around 500 nm. The characteristic linear emissions of Eu^{3+} ions are also observed benefiting from the energy transfer from $[\text{VO}_4]^{3-}$ to Eu^{3+} . Since the temperature quenching effect is more sensitive for the self-activated emission than that for the Eu^{3+} -related ones, the phosphor can be applied as a luminescent temperature sensor, with the absolute and relative temperature sensitivities of 0.012 K^{-1} and $1.56\% \text{ K}^{-1}$, respectively.

Received 21st October 2022
Accepted 9th December 2022

DOI: 10.1039/d2ra06647e

rsc.li/rsc-advances

Introduction

Phosphor-converted white light emitting diodes (WLEDs), known as fourth generation lighting sources, have attracted a lot of attention for their advantages of high efficiency, no mercury pollution, low carbon emissions, long life, small size, energy-saving and so on.^{1,2} Since human vision is not sensitive to UV light, the search for LED phosphors excited by UV and near-UV light has become a research hotspot.

Metal vanadate materials with different crystal structures exhibit various physical and chemical properties and are good phosphor host materials.^{3,4} Under the excitation of UV light, vanadate can produce a bright self-activation broad emission band in the wavelength range of 400–800 nm originating from the charge transfer (CT) transition of the $[\text{VO}_4]$ tetrahedron.^{5–8} The specific emission color/wavelength is mainly determined by certain metal ions and the crystal structure of the vanadates.^{9–11}

Garnet structure-based vanadate phosphors usually exhibit a self-activated blue-green emission. The garnet structure belongs to the cubic crystal system, described by the general formula $\text{A}_3\text{B}_2\text{C}_3\text{O}_{12}$ with a space group $Ia\bar{3}d$ (230).^{12,13} So far, several garnet structured vanadates, such as

$\text{LiCa}_3\text{ZnV}_3\text{O}_{12}$,¹⁴ $\text{NaCa}_2\text{Mg}_2\text{V}_3\text{O}_{12}$,^{15,16} $\text{Ca}_2\text{KZn}_2(\text{VO}_4)_3$,¹⁷ and $\text{KCa}_2\text{Mg}_2\text{V}_3\text{O}_{12}$,¹⁸ have been reported for the self-activating luminescent emissions. To expand the luminescent property of the garnet-structured vanadate phosphors, various rare earth ions have been introduced into these hosts, resulting in several new luminescent systems, such as $\text{NaCa}_2\text{Mg}_2\text{V}_3\text{O}_{12}:\text{Sm}^{3+}$,¹⁹ $\text{Ca}_2\text{AgZn}_2\text{V}_3\text{O}_{12}:\text{Nb}^{5+}$,²⁰ $\text{CaZnV}_2\text{O}_7:\text{Eu}^{3+}$,²¹ and $\text{Ca}_2\text{KZn}_2\text{V}_3\text{O}_{12}:\text{Dy}^{3+}$.²²

Several questions should be discussed as the rare earth ions with characteristic luminescence being doped into hosts with self-activating emissions. First, how does the lattice distortion corresponding to the impurity ions affect the self-activated emission? Second, is there any energy transfer existing between the CT transition of the $[\text{VO}_4]$ tetrahedron and the energy-level transition of the doping rare earth ions? Third, the temperature effects on the two emissions. All these three questions are still not well solved, although they are so obvious and common in ion-doped self-activated luminescence systems.

In this work, self-activated $\text{LCZV}:\text{xEu}^{3+}$ ($\text{x} = 0\text{--}0.155$) phosphors were prepared by a solution combustion reaction. Trying to solve the above three questions, we would analyze the crystal structure of pure and Eu^{3+} -doped LCZV, and monitor the photoluminescence of all the samples at room and higher temperatures. The energy transfer pathways of the LCZV host induced by Eu^{3+} are also investigated in detail. Meanwhile, a series of color-tunable phosphors would be obtained, and the possibility of their application would be evaluated as LED devices and fluorescent temperature sensors.

School of Material Science and Engineering, University of Jinan, 250022, Jinan, China.
E-mail: mse_zhangay@ujn.edu.cn; mse_yangp@ujn.edu.cn

† Electronic supplementary information (ESI) available. See DOI: <https://doi.org/10.1039/d2ra06647e>

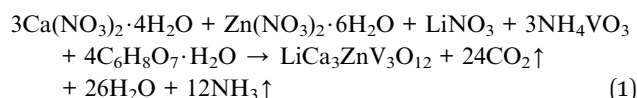


Experimental section

Synthesis of phosphors

The raw materials include calcium(II) nitrate ($\text{Ca}(\text{NO}_3)_2 \cdot 4\text{H}_2\text{O}$, 99.0%, Sinopharm), lithium(I) nitrate (LiNO_3 , 99.9%, Sinopharm), zinc(II) nitrate ($\text{Zn}(\text{NO}_3)_2 \cdot 6\text{H}_2\text{O}$, 98.0%, Damao Chemical Reagent Factory), europium(III) oxide (Eu_2O_3 , 99.99%, Macklin), ammonium metavanadate (NH_4VO_3 , 99.95%, Aladdin), and citric acid ($(\text{C}_6\text{H}_8\text{O}_7 \cdot \text{H}_2\text{O})$, 99.99%, Aladdin).

The chemical eqn (1) of $\text{LCZV}:\text{xEu}^{3+}$ phosphors preparation is as follows:^{23–25}



In a typical synthesis of LCZV phosphor, various nitrates were weighted according to the stoichiometric ratio in eqn (1), dissolved in the deionized water, and then mixed together. Appropriate amounts of NH_4VO_3 and citric acid were added in sequence to the mixed solution. After stirring for 10 min, an orange solution was obtained, which gradually changed to dark brown and finally to blue when heated to 80 °C. The pH value of the solution was adjusted with HNO_3 and $\text{NH}_3 \cdot \text{H}_2\text{O}$ solution. The prepared blue solution was transferred to a crucible, and the solution combustion reaction was carried out in air at 600 °C and kept for 20 min. The products were taken out after heat treatment and ground into fine powder.

For Eu^{3+} -doped LCZV phosphors, the experimental steps are exactly the same except that the raw materials are slightly adjusted according to their respective molecular formula.

Sample characterization

The X-ray powder diffraction (XRD) data of the samples were collected on an Ultima IV X-ray diffractometer (Rigaku, Japan) with Cu K α radiation ($\lambda = 1.5418 \text{ \AA}$) at a scanning rate of 5° min^{-1} in the range of 2θ from 15° to 80° at room temperature. Temperature-dependent XRD was acquired on a Smartlab X-ray diffractometer (Rigaku, Japan) with a temperature controller. Rietveld refinements of XRD patterns were conducted by general structure analysis programs to obtain the cell parameters and related information. The microstructure and chemical composition of the samples were analyzed by scanning electron microscopy (SEM) (Zeiss Gemini 300, Germany) and energy dispersive spectroscopy (EDS), respectively. The PL excitation (PLE) and PL spectra of the samples were obtained by a fluorescence spectrophotometer (Hitachi F-4600, Japan) with a xenon lamp of 150 W as an excitation source at room temperature. The PL decay curves of the samples were recorded by a steady-state/transient fluorescence spectrometer (Edinburgh Instruments FLS1000, Britain).

Fabrication of LED devices and temperature-dependent PL measurement

LED devices were fabricated by coating phosphors on a 310 nm UVB LED chip driven by 3.5 V and 40 mA using high refractive silicone ($A:B = 1:4$) as the binder.

The temperature-dependent PL characteristics of the samples were obtained by referring to the strategy in ref. 26 which was evaluated by heating the samples sealed in a metallic box and kept them at a particular temperature, and then rapidly transferring the sample at a specific temperature from the heater to the fluorescence spectrophotometer for measurement.

Results and discussion

Crystal structure and lattice distortion

The crystal structure model and coordinate environment of LCZV are shown in Fig. 1(a). LCZV has a garnet structure (space group $Ia\bar{3}d$ (230)) with the general formula $\text{A}_3\text{B}_2\text{C}_3\text{O}_{12}$,^{12,27} in which A is Ca^{2+} , B is Li^+ or Zn^{2+} , and C is V^{5+} . The whole structure is mainly composed of tetrahedron $[\text{VO}_4]$, dodecahedron $[\text{CaO}_8]$ and octahedron $[\text{ZnO}_6]$, wherein $[\text{ZnO}_6]$ form a regular octahedron structure are sharing borders and corners with $[\text{VO}_4]$ and $[\text{CaO}_8]$. The unit cell of the LCZV structure can be viewed as a connected network of dodecahedron, octahedron and tetrahedron.

Fig. 1(b) exhibits the XRD patterns of $\text{LCZV}:\text{xEu}^{3+}$ ($x = 0, 0.015, 0.045, 0.095$) samples. From Fig. 1(b), all the diffraction peaks of pure LCZV and $\text{LCZV}:\text{xEu}^{3+}$ samples with different Eu^{3+} -doping concentrations are well correlated with the standard card (JCPDS no. 24-1212),^{10,28} which indicates the formation of pure phase LCZV host and the absence of second phase related to the doping of Eu^{3+} .

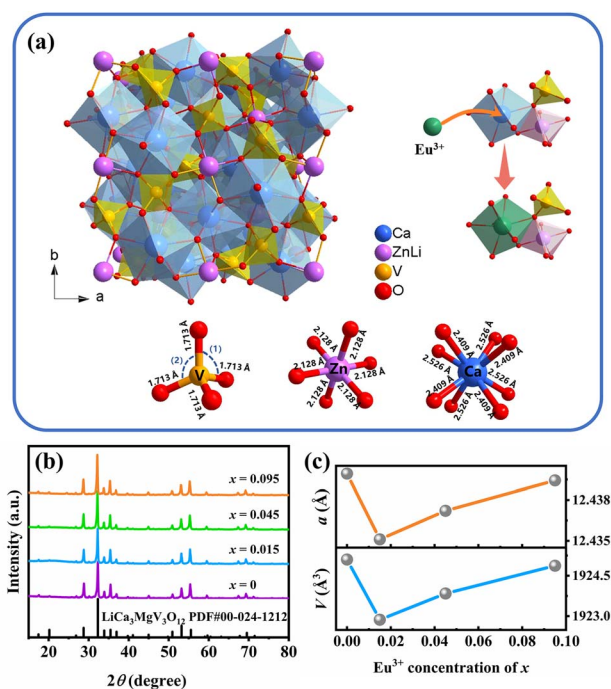


Fig. 1 (a) Crystal structure of LCZV (color balls: Ca blue, Zn/Li purple, V orange, O red) and coordinate environment of $[\text{VO}_4]$, $[\text{CaO}_8]$ and $[\text{ZnO}_6]$ from XRD refinement. (b) XRD patterns ($2\theta = 15\text{--}80^\circ$) of $\text{LCZV}:\text{xEu}^{3+}$ ($x = 0, 0.015, 0.045, 0.095$) samples. (c) The cell parameters (a , V) of $\text{LCZV}:\text{xEu}^{3+}$ samples varying with Eu^{3+} concentration.



Table 1 Ionic radii difference percentage (D_r) between host cations and Eu^{3+}

Host cation (CN)	Doped ion (CN)	R_m (Å)	R_d (Å)	D_r (%)
Ca^{2+} (8)	Eu^{3+} (8)	11.20	10.66	4.82
Zn^{2+} (6)	Eu^{3+} (6)	7.40	9.47	27.97
Li^+ (6)	Eu^{3+} (6)	7.60	9.47	24.61

Davolos' research shows that efficient ion substitution can be achieved when the ionic radii difference percentage (D_r) between dopant ions and replaced ions is within 30%. D_r can be estimated by eqn (2):⁸

$$D_r = 100 \times \frac{R_m(\text{CN}) - R_d(\text{CN})}{R_m(\text{CN})} \quad (2)$$

where CN represents the coordination number, R_d and R_m are the ionic radii of dopant ions (Eu^{3+}) and host cations (Li^+ , Zn^{2+} , Ca^{2+}) respectively. The calculated results of D_r are listed in Table 1, which confirms that Eu^{3+} will occupy part of the Ca^{2+} sites.

To further verify the phase purity and Eu^{3+} doping sites of the designed samples, the XRD patterns of $\text{LCZV}:\text{xEu}^{3+}$ ($x = 0, 0.015, 0.045, 0.095$) samples were fitted by the Rietveld refinement method (the results are shown in Fig. S1†) to optimize the initial crystal structure of the samples. The good R -factors and χ values are shown in Table S1,† and the detailed atomic coordinates are listed in Table S2.† Table 2 shows the bond length and angles obtained from XRD refinement. It can be observed that V^{5+} and Ca^{2+} ions have complicated bond lengths, and two kinds of angles $\text{O}-\text{V}-\text{O}^{(1)}$ and $\text{O}-\text{V}-\text{O}^{(2)}$ can also be seen in $[\text{VO}_4]$. The coordinate environment of metal-oxygen polyhedrons obtained is also exhibited in Fig. 1(a).

By analyzing the cell parameters (a , V) of the samples in Table S1,† it can be found that the introduction of Eu^{3+} ions led to a shrinkage of the LCZV lattice. This lattice contraction coincides with the inference that partial Ca^{2+} sites are occupied by Eu^{3+} ions with smaller ionic radius. From Fig. 1(c) drawn according to Table S1,† it is obvious that the cell parameter of $\text{LCZV}:\text{xEu}^{3+}$ ($x = 0, 0.015, 0.045, 0.095$) samples almost linearly increased with Eu^{3+} ions concentration which deviated from Vegard's law, although the cell parameter of all the doped

samples are smaller than that of pure one. This increasing trend of the cell parameter with Eu^{3+} concentration can be attributed to the generation of interstitial oxygen for the purpose of charge balance, which has been broken when the trivalent Eu^{3+} ions occupied the divalent Ca^{2+} ion sites.

Table 2 summarizes the average interatomic distance and $\text{O}-\text{V}-\text{O}$ bond angle of the $\text{LCZV}:\text{xEu}^{3+}$ ($x = 0, 0.015, 0.045, 0.095$) samples, which show various changes with the increase of Eu^{3+} concentration. Among them, the decrease of the $\text{Ca}-\text{O}$ bond length led to the lattice contraction of the $[\text{CaO}_8]$ dodecahedron; the increase of the $\text{V}-\text{O}$ bond length and the change of the two kinds of $\text{O}-\text{V}-\text{O}$ bond angles resulted in the lattice expansion of the $[\text{VO}_4]$ tetrahedron, which squeezes the $\text{Zn}-\text{O}$ bond length at the adjacent $[\text{ZnO}_6]$ octahedra to relieve the lattice strain. This lattice expansion with the increase of Eu^{3+} doping concentration gives another evidence for the existence of interstitial oxygen. These phenomena further prove that Eu^{3+} successfully replaces Ca^{2+} and occupies the lattice sites.

It can be seen from Fig. 2(a) and S2† that LCZV samples show similar micromorphology before and after Eu^{3+} doping, although the particle sizes of the samples decrease with Eu^{3+} doping concentration. All samples are composed of particles with holes and adhered to each other. Based on this morphology, we deduced the growth mechanism of LCZV. After ignition at 600°C , the combustion reaction of the precursor will release a lot of heat, instantly generating a very high temperature inside the sample. Under such high temperatures, the precursor decomposes, LCZV nucleates and grows rapidly (according to the reaction eqn (1)). Since the process of nucleation and growth is very fast, the particles stick together and show the morphology of adhesion. At the same time, a large amount of gas is released due to the burning of organic fuel (citric acid) in this process, which explains the appearance of holes in LCZV particles. The elemental composition of $\text{LCZV}:0.015\text{Eu}^{3+}$ has been characterized by EDS and the results are shown in Fig. 2(b) and (c). From Fig. 2(b), the elements of Ca, Zn, V, and Eu all exhibit uniform distribution, indicating homogeneous doping of Eu ions. The EDS image (Fig. 2(c))

Table 2 Inter-atomic distances and $\text{O}-\text{V}-\text{O}$ bond angles of $\text{LCZV}:\text{xEu}^{3+}$ ($x = 0, 0.015, 0.045, 0.095$) samples calculated from XRD refinement result^a

Sample (x)	Bond distances (Å)				Bond angles ($^\circ$)	
	Ca-O	Zn-O	V-O	V-V	$\text{O}-\text{V}-\text{O}^{(1)}$	$\text{O}-\text{V}-\text{O}^{(2)}$
0	2.468	2.128	1.713	3.809	114.05	100.70
0.015	2.462	2.124	1.730	3.807	113.37	101.92
0.045	2.462	2.126	1.724	3.808	113.77	101.18
0.095	2.463	2.128	1.718	3.808	113.74	101.24

^a $\text{O}-\text{V}-\text{O}^{(1)}$ and $\text{O}-\text{V}-\text{O}^{(2)}$ represent two symmetric vanadium-oxygen bond angles in $[\text{VO}_4]$ respectively, and the angle variation trend between $\text{O}-\text{V}-\text{O}^{(1)}$ and $\text{O}-\text{V}-\text{O}^{(2)}$ is inversely proportional.

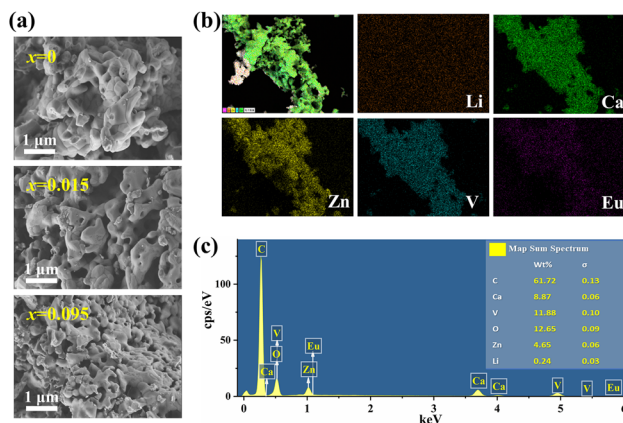


Fig. 2 (a) SEM images of $\text{LCZV}:\text{xEu}^{3+}$ ($x = 0, 0.015, 0.095$). (b) Elemental mapping images of $\text{LCZV}:0.015\text{Eu}^{3+}$. (c) EDS pattern (inset shows the elemental wt% distribution) of $\text{LCZV}:0.015\text{Eu}^{3+}$.



revealed all elements present in the sample, including small peaks of lower energy due to Eu^{3+} doping and a carbon peak caused by the use of carbon ribbons in the sample preparation.¹⁷

The self-activated luminescence and Eu^{3+} -related luminescence

PLE and PL spectra of pure LCZV and $\text{LCZV}:\text{xEu}^{3+}$ phosphors are shown in Fig. 3. As shown in Fig. 3(a), the PLE spectrum of pure LCZV measured with an emission wavelength of 500 nm is an excitation band centered at 322 nm. The PL spectrum measured under 322 nm UV-light excitation ranges from 400 to 750 nm, with a peak at 500 nm, and a full width at half maximum (FWHM) close to 121 nm. By using the Gaussian fitting, the emission band can be deconvoluted into two sub-bands around 491 nm and 557 nm, and the excitation band into two sub-bands around 278 nm and 324 nm. The luminescence of pure LCZV is attributed to the self-activated CT transitions of the $[\text{VO}_4]^{3-}$ groups,^{11,29} which is described on the left in Fig. 4. Under the excitation of UV light, the electrons in the ground state $^1\text{A}_1$ absorb energy and transition to the excited state $^1\text{T}_1$ or $^1\text{T}_2$ (corresponding to the excitation peaks at 278 nm and 324 nm), then relax to $^3\text{T}_1$ or $^3\text{T}_2$ through a non-radiative transition, and finally decay to the ground state $^1\text{A}_1$ and emit light around 491 nm ($^3\text{T}_2 \rightarrow ^1\text{A}_1$) and 557 nm ($^3\text{T}_1 \rightarrow ^1\text{A}_1$).

As shown in Fig. 3(b), the PL spectrum of $\text{LCZV}:\text{0.015Eu}^{3+}$ phosphor collected under 310 nm excitation exhibits both the self-activated luminescence of $[\text{VO}_4]^{3-}$ groups around 500 nm and the characteristic linear emission of the 4f–4f transition of Eu^{3+} ions at 594, 613, 634 and 711 nm (corresponding to the transitions of $^5\text{D}_0 \rightarrow ^7\text{F}_j$ ($j = 1-4$)).³⁰ The PLE spectrum is obtained by monitoring the $^5\text{D}_0 \rightarrow ^7\text{F}_2$ characteristic emission of Eu^{3+} ions at 613 nm, which contains a charge transfer band (CTB) from 200 to 350 nm and two characteristic excitation peaks of Eu^{3+} from 350 to 500 nm. The maximum value of the CTB is 310 nm which can be attributed to the CT transition

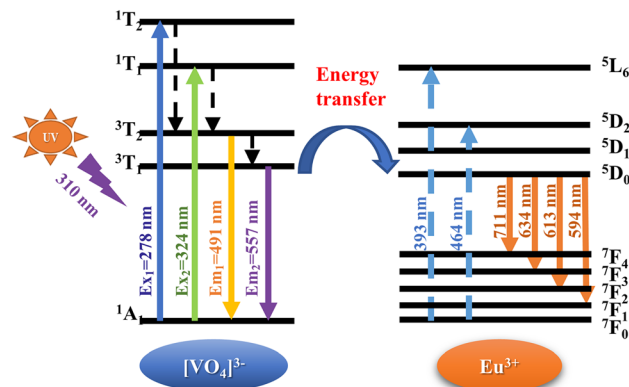


Fig. 4 The energy transfer process from $[\text{VO}_4]^{3-}$ groups to Eu^{3+} ions.

($\text{V}^{5+} \rightarrow \text{O}^{2-}$) of $[\text{VO}_4]^{3-}$ groups. The sharp peaks around 393 and 464 nm are attributed to the $^7\text{F}_0 \rightarrow ^5\text{L}_6$ and $^7\text{F}_0 \rightarrow ^5\text{D}_2$ transitions of the trivalent Eu^{3+} dopant. The intensity of CTB at 310 nm is obviously higher than those of $^7\text{F}_0 \rightarrow ^5\text{L}_6$ and $^7\text{F}_0 \rightarrow ^5\text{D}_2$ transitions of Eu^{3+} at 393 and 464 nm. It can be inferred that there must be an effective energy transfer between $[\text{VO}_4]^{3-}$ groups and Eu^{3+} ions. The simplified energy transfer process between $[\text{VO}_4]^{3-}$ and Eu^{3+} ions is shown in Fig. 4. Under the 310 nm UV excitation, the $[\text{VO}_4]^{3-}$ groups are excited through the $\text{V}^{5+} \rightarrow \text{O}^{2-}$ CTB, when Eu^{3+} ions were introduced into the system, efficient energy transfer from $[\text{VO}_4]^{3-}$ groups to the Eu^{3+} excited states $^5\text{D}_0$, eventually resulting in radiative transitions of $^5\text{D}_0 \rightarrow ^7\text{F}_j$ ($j = 1-4$). It can also be noted from Fig. 3(b) that the dominant emission peak of Eu^{3+} is at 613 nm due to the $^5\text{D}_0 \rightarrow ^7\text{F}_2$ transition, indicating that Eu^{3+} ions in LCZV host are located in a non-inversion symmetry position according to the Judd–Ofelt theory.³¹ This result agrees well with the conclusion that Eu^{3+} takes on the Ca^{2+} sites (without inversion symmetry) in LCZV crystal structure.

A series of $\text{LCZV}:\text{xEu}^{3+}$ ($x = 0-0.155$) samples were synthesized to further examine the effect of Eu^{3+} doping concentration on the PL properties of the phosphors. As shown in Fig. 5, under excitation at 310 nm, the characteristic emission peaks of all samples are similar, and the PL emission intensity changes

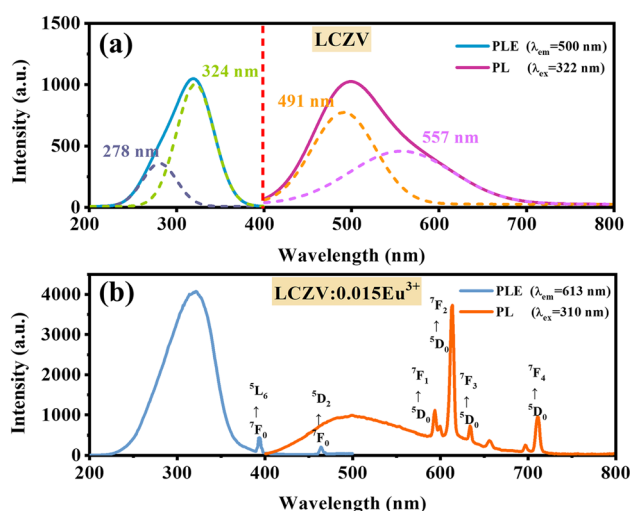


Fig. 3 The PLE and PL spectra of (a) LCZV and (b) $\text{LCZV}:\text{0.015Eu}^{3+}$ phosphors.

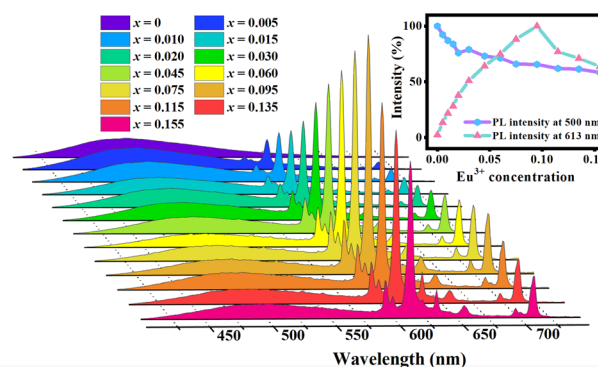


Fig. 5 The emission spectra of $\text{LCZV}:\text{xEu}^{3+}$ ($x = 0-0.155$) under 310 nm excitation. The inset depicts the PL relative intensities at 500 nm and 613 nm as a function of Eu^{3+} concentration.



significantly with the increase of the Eu^{3+} doping amount. The inset of Fig. 5 shows the relative PL intensity of the $\text{LCZV}:\text{xEu}^{3+}$ ($x = 0-0.155$) samples as a function of Eu^{3+} concentration. When the concentration of Eu^{3+} ion is lower than 0.095, with the increase of Eu^{3+} ion concentration, the self-activated emission around 500 nm shows a decrease in intensity, while the Eu^{3+} -related emission shows an increase, which confirms the conclusion that there is an effective energy transfer from $[\text{VO}_4]^{3-}$ groups to Eu^{3+} ions. It is worth noting that the intensity of the self-activated emission first shows a rapid decrease and then turns to a slow decrease, with the inflection point around 0.02, at which the most obvious lattice distortion occurs according to Fig. 1(c). It can be inferred that Eu^{3+} ions would not only transfer the energy absorbed by $[\text{VO}_4]^{3-}$ groups, but also the lattice contraction caused by Eu^{3+} ions weaken the self-activated luminescence of $[\text{VO}_4]^{3-}$ groups.

As the concentration of Eu^{3+} ions exceeds 0.095, the Eu^{3+} -related emission does not increase but decreases. According to the previous literature,³² the concentration quenching occurs from the non-radiative energy migration (short-range exchange interactions or long-range multipolar interactions) among the luminescence activators. Blasse pointed out that when the critical transfer distance (R_c) between Eu^{3+} is less than or equal to 5 Å, the concentration quenching phenomenon is attributed to exchange interaction; otherwise, it is attributed to multipolar interactions. The value of R_c can be calculated by the following formula:³³

$$R_c = 2 \left(\frac{3V}{4\pi x_c Z} \right)^{1/3} \quad (3)$$

where R_c is the critical distance, V refers to the volume of the unit cell, x_c is the critical doping concentration, and Z is the number of substitutable cations in a unit cell. For the LCZV host, the lattice parameter is as follows: $a = 12.43993$ Å; $V = 1925.101$ Å³; $x_c = 0.095$; and $Z = 8$. Substituting these data into formula (3), the value of R_c is 16.91 Å, which was higher than 5 Å. Therefore, multipolar interactions would be the dominant energy transfer mechanism between Eu^{3+} ions in the LCZV host.

Fig. 6 shows the room temperature luminescence decay curves of $[\text{VO}_4]^{3-}$ groups at 500 nm for LCZV and $\text{LCZV}:\text{0.015Eu}^{3+}$ samples, respectively. The fluorescence decay curves of $[\text{VO}_4]^{3-}$ fit well with the bi-exponential fitting eqn (4):^{34,35}

$$I(t) = I_0 + A_1 \exp(-t/\tau_1) + A_2 \exp(-t/\tau_2) \quad (4)$$

In the formula, $I(t)$ represents the luminescent intensity at time t , t is the radiation decay time, τ_1 and τ_2 are the short and long PL lifetime, and A_1 and A_2 are fitting constants. The calculation formula of average excited state life (τ_{avg}) is shown in eqn (5):³⁶

$$\tau_{\text{avg}} = (A_1 \tau_1^2 + A_2 \tau_2^2) / (A_1 \tau_1 + A_2 \tau_2) \quad (5)$$

The calculated fluorescence decay parameters of the $\text{LCZV}:\text{xEu}^{3+}$ ($x = 0, 0.015$) samples are listed in Table 3. As shown in Table 3, the average fluorescence lifetime of the self-

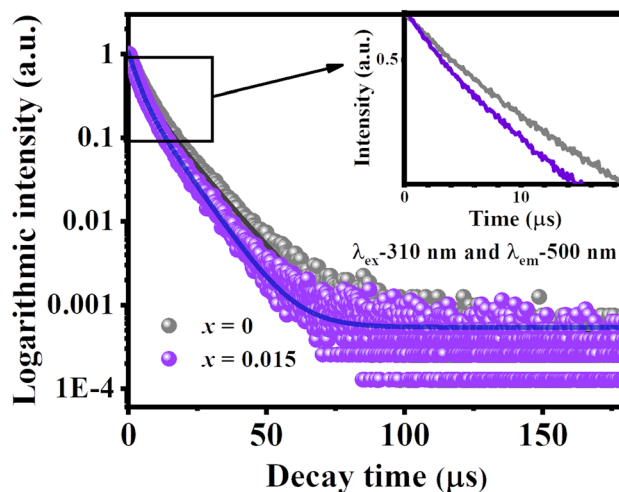


Fig. 6 The PL decay lifetimes of $[\text{VO}_4]^{3-}$ groups at 500 nm for $\text{LCZV}:\text{xEu}^{3+}$ ($x = 0, 0.015$).

activated emission is shortened after doping with Eu^{3+} ions. By discussing the parameters of the fast decay mechanism (τ_1 , A_1) and the slow decay mechanism (τ_2 , A_2) in detail, it can be found that after Eu^{3+} doping, both the decay times of the fast component (τ_1) and the slow component (τ_2) are shortened, and the weight of the fast component (A_1) is relatively increased while the weight of the slow component (A_2) is relatively decreased. We mainly attribute the shortening of the decay time of the two components to the reduction of the radiative transition probability of the $[\text{VO}_4]^{3-}$ groups caused by the energy transfer to Eu^{3+} ; while the change in the weight of the two components is attributed to the variation of the ratio between the two transition mechanisms (${}^3\text{T}_1 \rightarrow {}^1\text{A}_1$, ${}^3\text{T}_2 \rightarrow {}^1\text{A}_1$) due to the lattice distortion caused by Eu^{3+} doping. Comparing the changes in the decay time and the weight of the two components, it can be judged that the effect of Eu^{3+} ions doping on lattice distortion is smaller than that of energy transfer.

Fig. 7 and Table S3† show the CIE chromaticity coordinates of $\text{LCZV}:\text{xEu}^{3+}$ ($x = 0-0.155$) samples. Fig. S3† shows the variation of the chromaticity coordinates x and y with the Eu^{3+} doping concentration. Obviously, with the increase of Eu^{3+} concentration, the chromaticity gradually transitions from bluish-green (0.2039, 0.2421) to white (0.2739, 0.3145) and then to orange-red (0.3634, 0.4014). Color tunable phosphors were thus obtained by changing the doping concentration of Eu^{3+} in $\text{LCZV}:\text{xEu}^{3+}$ ($x = 0-0.155$) samples. In particular, white emissions were achieved when the value of x was set as 0.015. The packaged multicolor LED devices were displayed in the inset of

Table 3 PL decay parameters of the $[\text{VO}_4]^{3-}$ groups in $\text{LCZV}:\text{xEu}^{3+}$ ($x = 0, 0.015$) samples

Sample (x)	A_1	τ_1 (μs)	A_2	τ_2 (μs)	χ^2	τ_{avg} (μs)
0	5.39	4.55	2.65	12.17	1.205	8.93
0.015	5.45	3.68	2.05	10.68	1.069	7.33

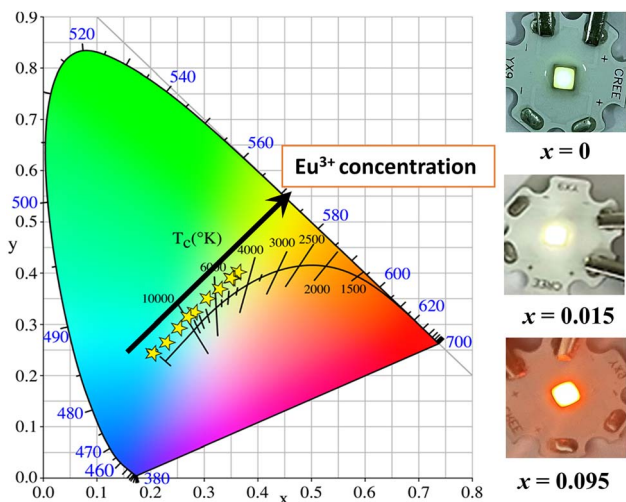


Fig. 7 CIE chromaticity coordinates of LCZV: $x\text{Eu}^{3+}$ ($x = 0\text{--}0.155$) (left) and the LED device of samples irradiated with a 310 nm UV lamp (right).

Fig. 7. The calculated correlation color temperature (CCT) values are listed in Table S3.† For the white-emitting LCZV:0.015 Eu^{3+} phosphor, CCT is about 7683 K. Generally speaking, we obtained a series of color tunable phosphors by doping Eu^{3+} ions into the self-activating luminescent LCZV host, and white light was achieved when the Eu^{3+} doping concentration was 0.015 and the multicolor LED devices were fabricated with multicolor luminescent effect.

Temperature-dependent PL properties

Fig. 8 depicts the temperature-dependent PL spectra of LCZV:0.015 Eu^{3+} under 310 nm light excitation. It can be found that the positions and shapes of characteristic emission peaks of samples at different temperatures from 293 K to 473 K are similar, and the PL emission intensity decreases with the increase in temperature. The inset in Fig. 8 describes the relative PL intensity curve with temperature. It can be seen that under ultraviolet

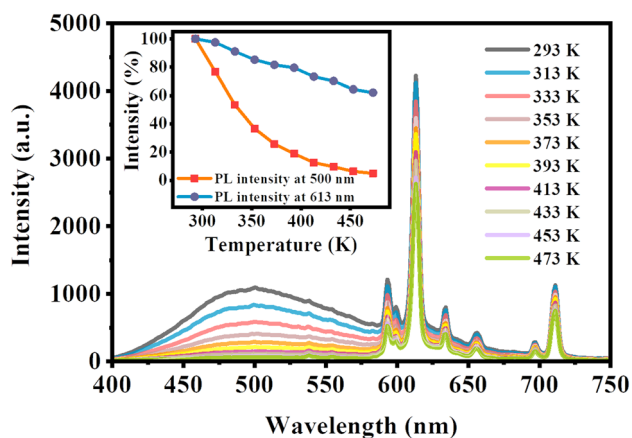


Fig. 8 The temperature-dependent PL spectra of LCZV:0.015 Eu^{3+} . The inset depicts the temperature-dependent PL relative intensities at 500 nm and 613 nm.

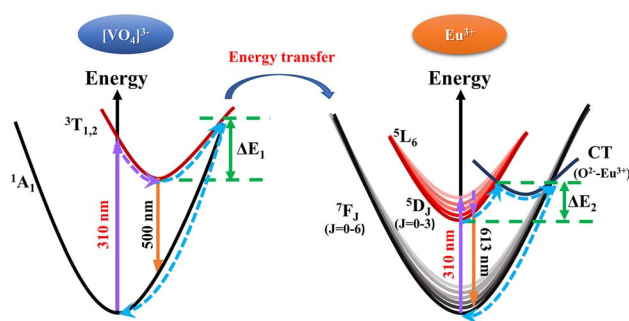


Fig. 9 Schematic configuration coordinate diagram for thermal-quenching of $[\text{VO}_4]^{3-}$ groups and Eu^{3+} ions in LCZV host.

excitation at 310 nm, the emission intensity of $[\text{VO}_4]^{3-}$ groups at 500 nm decreased sharply to 4.9% of the initial value with increasing temperature; while the emission intensity of Eu^{3+} ions at 613 nm only drops to 62.1% of its initial value. As shown in the inset of Fig. 8, the luminescence intensity of $[\text{VO}_4]^{3-}$ groups is more sensitive to temperature than that of Eu^{3+} .

The thermal-quenching of $[\text{VO}_4]^{3-}$ groups and Eu^{3+} ions in LCZV:0.015 Eu^{3+} phosphor can be explained by the schematic configuration coordinate diagram shown in Fig. 9.^{6,37} In general, under the excitation of 310 nm light, the energy absorbed by the $[\text{VO}_4]^{3-}$ groups emitted broadband cyan light through the CT transition between excited states $^3\text{T}_{1,2}$ and ground state $^1\text{A}_1$. In the presence of Eu^{3+} ions, the energy transfer occurs from the excited $[\text{VO}_4]^{3-}$ groups to Eu^{3+} ions. The outer electrons of Eu^{3+} are first excited to the high-level state $^5\text{L}_6$, then relaxed to the $^5\text{D}_0$ level through a non-radiative transition, and finally return to the $^7\text{F}_6$ ground state, with the emission of the characteristic Eu^{3+} -related spectrum. As the temperature increases, the excited electrons of $[\text{VO}_4]^{3-}$ groups absorb additional vibrational energy and cross the barrier ΔE_1 to the intersection of $^3\text{T}_{1,2}$ and $^1\text{A}_1$ states, and rapidly relax to ground state $^1\text{A}_1$ by non-radiative transition. Meanwhile, part of electrons at the $^5\text{D}_0$ level of Eu^{3+} absorbed energy, surmounted the activation energy barrier ΔE_2 by phonon-electron coupling^{38,39} to the intersection of $^5\text{D}_0$ and $^7\text{F}_6$, and finally back to the ground state through non-radiative transition.^{32,37,40} In summary, as the temperature increases, the thermal vibration of the matrix lattice is enhanced, and the phonons in the crystal increase, leading to the enhanced probability of the multiphonon relaxation process. The interaction between electrons and phonons is thus enhanced, resulting in the thermal quenching.^{41,42}

To further study the thermal quenching process of the self-activated luminescence from $[\text{VO}_4]^{3-}$ groups, we conducted the temperature-dependent XRD patterns and the PL decay lifetimes as a function of temperature. Fig. 10(a) shows the XRD patterns of LCZV:0.015 Eu^{3+} at different temperatures (298–473 K). It can be found that pure host phase remains at different temperatures, indicating that the crystal structure of the sample has good thermal stability from room temperature to 473 K. However, an enlarged XRD pattern at $2\theta = 32\text{--}32.5^\circ$ indicates that the diffraction peaks of the samples shift to lower angles with the increase of temperature, which means that the LCZV:0.015 Eu^{3+} sample has positive thermal expansion properties.

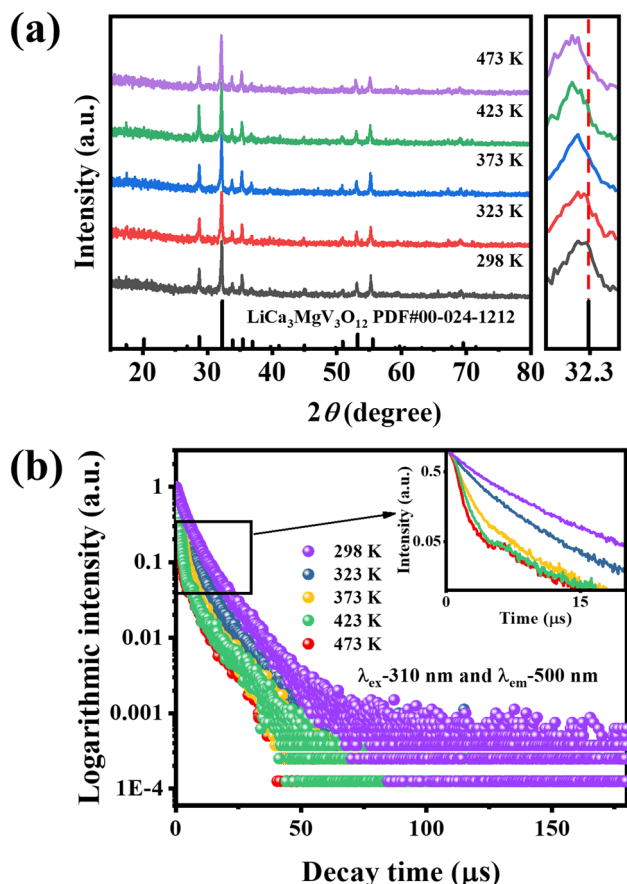


Fig. 10 (a) The temperature-dependent XRD patterns ($2\theta = 15\text{--}80^\circ$) and enlarged XRD patterns ($2\theta = 32\text{--}32.5^\circ$) of LCZV:0.015Eu³⁺ (298–473 K). (b) The PL decay lifetimes of LCZV:0.015Eu³⁺ at different temperatures (293–473 K).

Fig. 10(b) shows the PL decay curves of the LCZV:0.015Eu³⁺ sample at different temperatures (298–473 K), measured with the excitation wavelength of 310 nm and the emission wavelength of 500 nm. It can be seen that the lifetime of the self-activated PL shortens with increasing temperature. The average decay times τ_{avg} of [VO₄]^{3−} groups at different temperatures are calculated according to eqn (5) and shown in Table 4. From Table 4, a shortening trend is observed with increasing temperature, both for the fast decay mechanism (τ_1) and the slow decay mechanism (τ_2), due to the thermal quenching effect shown in Fig. 9. At the same time, we also found that with the increase in temperature, the proportion of the fast decay mechanism (A_1) is gradually increasing while the proportion of slow decay mechanisms (A_2) is gradually decreasing. This change of the fluorescence decay mechanism may be attributed to the lattice-expansion caused by heating (as described in Fig. 10(a)).

The activation energy ΔE of thermal quenching process was calculated by using the Arrhenius equation:^{35,37,43}

$$I = \frac{I_0}{1 + A \exp(-\Delta E/kT)} \quad (6)$$

where I_0 is the emission intensity at initial room temperature, I is the emission intensity at monitored temperature, A is

Table 4 PL decay parameters of the [VO₄]^{3−} groups of LCZV:0.015Eu³⁺ sample at different temperatures

T (K)	A_1	τ_1 (μs)	A_2	τ_2 (μs)	χ^2	τ_{avg} (μs)
298	5.45	3.68	2.05	10.68	1.205	7.33
323	5.69	2.81	1.13	9.49	1.069	5.49
373	9.04	1.39	0.72	8.46	1.052	3.70
423	9.17	1.23	0.42	7.35	1.022	2.55
473	10.15	1.18	0.25	6.26	1.014	1.77

constant, ΔE is the activation energy and k stands for the Boltzmann constant.⁴³ As shown in Fig. S4,[†] the thermal stability data of LCZV:0.015Eu³⁺ phosphor can be fitted well by using eqn (6). According to the slope estimation, the thermal quenching activation energy ΔE values for [VO₄]^{3−} groups and Eu³⁺ are 0.510 eV and 0.358 eV, respectively. The difference in the value of ΔE between the [VO₄]^{3−} groups and the Eu³⁺ ions indicates that they have different responses to temperature changes.

The variation of the relative intensity of the two emissions (around 500 nm and 613 nm) results in a change of the emitting light color with temperature. As displayed by the CIE chromaticity diagrams in Fig. 11, the luminescence color of LCZV:0.015Eu³⁺ sample gradually changes from white to orange-red as the ambient temperature increases from 293 K to 473 K. As shown in Fig. S5,[†] CIE x and CIE y of the sample exhibit a linear increasing trend with the rising temperature. All of these results demonstrate that the LCZV:0.015Eu³⁺ phosphor has potential to be used as a luminescent temperature sensor, which is a device that can determine the real-time temperature through the luminescent color.

In order to evaluate the performance of the sample as a fluorescent temperature sensor, it is necessary to characterize the following parameters, fluorescence intensity ratio (FIR), absolute sensitivity (S_a) and relative sensitivity (S_r). The

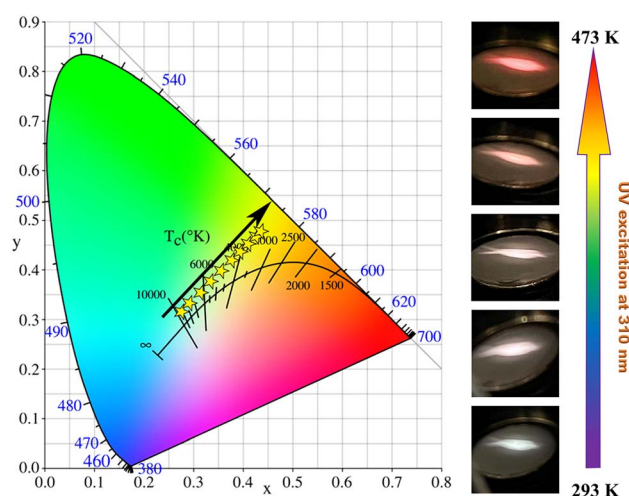


Fig. 11 The CIE chromaticity diagrams of LCZV:0.015Eu³⁺ at different temperatures (left) and the luminescent images under 310 nm excitation (right).

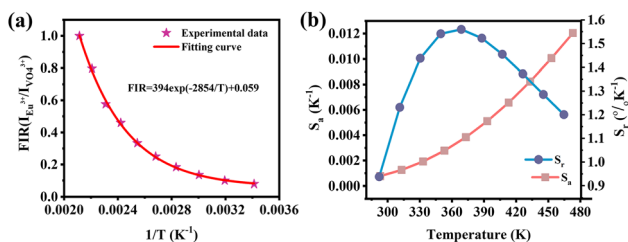


Fig. 12 (a) FIR values monitored at different temperatures of LCZV:0.015Eu³⁺. (b) S_a and S_r values monitored at different temperatures of LCZV:0.015Eu³⁺.

temperature-dependent FIR values can be obtained by fitting the experimental data according to the following eqn (7):²⁹

$$\text{FIR} = \frac{I_{\text{Eu}^{3+}}}{I_{[\text{VO}_4]^{3-}}} = \frac{I_{0,\text{Eu}^{3+}}}{I_{0,[\text{VO}_4]^{3-}}} \frac{1 + A_{[\text{VO}_4]^{3-}} \exp\left(-\frac{\Delta E_{[\text{VO}_4]^{3-}}}{kT}\right)}{1 + A_{\text{Eu}^{3+}} \exp\left(-\frac{\Delta E_{\text{Eu}^{3+}}}{kT}\right)} \approx B + C \exp(-E/kT) \quad (7)$$

where B , C and E are constants associated with the I_0 , A and ΔE of Eu³⁺ ions and [VO₄]^{3−} groups. The estimated FIR values can be well-matched with the fitting curve based on eqn (7). The results of FIR values at various temperatures are shown in Fig. 12(a). As the temperature rises from 293 to 473 K, the FIR values for the LCZV:0.015Eu³⁺ phosphor decrease sharply.

The temperature sensitivity of the LCZV:0.015Eu³⁺ sample was investigated by the absolute sensitivity (S_a) and relative sensitivity (S_r), which can be calculated through the following equations:⁴⁴

$$S_a = \frac{d(\text{FIR})}{dT} = C \exp\left(\frac{-E}{kT}\right) \left(\frac{E}{kT^2}\right) \quad (8)$$

$$S_r = 100\% \times \frac{1}{\text{FIR}} \frac{d(\text{FIR})}{dT} = 100\% \times \frac{C \exp(E/kT)}{B + C \exp(-E/kT)} \times \frac{E}{kT^2} \quad (9)$$

S_a and S_r values of the LCZV:0.015Eu³⁺ phosphor at different temperatures deduced by eqn (8) and (9) are shown in Fig. 12(b). S_a is a crucial coefficient to assess the FIR change rate, which is a sign to measure the response-ability of the optical temperature sensor to temperature change. The samples with higher S_a may be more suitable for temperature sensing.⁸ It was clear that the value of S_a showed a strong upward trend with the increase of temperature and achieved the maximum value of 0.012 K^{−1} at about 473 K. Whereas the S_r value initially grew up to the maximum (1.560% K^{−1}) at 373 K, and then decreased with the further increase of temperature. The obtained samples showed higher S_a and S_r values, indicating that the LCZV:0.015Eu³⁺ phosphor obtained in this work is a promising candidate for remote non-invasive optical thermometers using fluorescence intensity ratio technology.

Conclusions

Eu³⁺ ions were introduced into the lattice of LCZV to study the interaction of the self-activated and dopant-related

luminescence. The lattice distortion caused by Eu³⁺ was evaluated in terms of bond lengths and bond angles, which corresponded to the decrease of self-activated fluorescence intensity. Both the self-activated and Eu³⁺-related emissions were detected, attributed to the effective energy transfer from [VO₄]^{3−} groups to Eu³⁺ ions. The difference of the thermal stability of the two emissions led to suitable temperature sensing characteristics. Based on the above results, the following products can be developed: color-tunable phosphors, a white light emitting LED, and a luminescent temperature sensor for non-contact test system.

Conflicts of interest

There are no conflicts to declare.

Acknowledgements

This work was supported in part by the projects from National Natural Science Foundation of China (51302106, 51501071, 21071061) and Outstanding Young Scientists Foundation Grant of Shandong Province (BS2010CL004).

References

- 1 J. Yang, P. He, Y. Xie, Q. Chen, Q. Dong, W. Nie, F. Yang, W. Wang, F. Du, J. Peng and X. Ye, *J. Alloys Compd.*, 2022, **903**, 163815.
- 2 M. Xu, C. Fan, C. Yang, K. Song, F. Hussain, W. Sheng, J. Wu, H. Wang, W. Su, Q. Huang and S. Sun, *J. Lumin.*, 2021, **237**, 118197.
- 3 T. Nakajima, M. Isobe, T. Tsuchiya, Y. Ueda and T. Kumagai, *J. Lumin.*, 2009, **129**, 1598–1601.
- 4 M. K. Mahata, K. Kumar and V. K. Rai, *Sens. Actuators, B*, 2015, **209**, 775–780.
- 5 T. Nakajima, M. Isobe, T. Tsuchiya, Y. Ueda and T. Manabe, *J. Phys. Chem. C*, 2010, **114**, 5160–5167.
- 6 F. Kang, Y. Du, P. Boutinaud, G. Sun, X. Wang, J. Lu and S. Xiao, *Adv. Mater.*, 2020, **1**, 2467–2482.
- 7 L. Li, X. G. Liu, H. M. Noh and J. H. Jeong, *J. Solid State Chem.*, 2015, **221**, 95–101.
- 8 H. Zhou, N. Guo, X. Lü, Y. Ding, L. Wang, R. Ouyang and B. Shao, *J. Lumin.*, 2020, **217**, 116758.
- 9 M. Y. Espinosa-Cerón, A. N. Meza-Rocha, S. Carmona-Téllez, C. Chacón, O. Soriano-Romero and R. Lozada-Morales, *J. Lumin.*, 2021, **238**, 118239.
- 10 X. Huang and H. Guo, *Ceram. Int.*, 2018, **44**, 10340–10344.
- 11 Y. Matsushima, T. Koide, M. Hiro-Oka, M. Shida, A. Sato, S. Sugiyama, M. Ito and J. McKittrick, *J. Am. Ceram. Soc.*, 2015, **98**, 1236–1244.
- 12 T. Hasegawa, Y. Abe, A. Koizumi, T. Ueda, K. Toda and M. Sato, *Inorg. Chem.*, 2018, **57**, 857–866.
- 13 H. Zhou, W. Sun, X. Liu, K. Wang, H. Ruan and X. Chen, *Ceram. Int.*, 2019, **45**, 2629–2634.
- 14 X. Huang and H. Guo, *RSC Adv.*, 2018, **8**, 17132–17138.
- 15 X. Chen, Z. Xia, M. Yi, X. Wu and H. Xin, *J. Phys. Chem. Solids*, 2013, **74**, 1439–1443.



- 16 D. Pasinski and J. Sokolnicki, *Materials*, 2020, **13**, 2996.
- 17 L. K. Bharat, S. K. Jeon, K. G. Krishna and J. S. Yu, *Sci. Rep.*, 2017, **7**, 42348.
- 18 X. Huang, S. Wang, S. Rtimi and B. Devakumar, *J. Photochem. Photobiol. A*, 2020, **401**, 112765.
- 19 R. Cao, X. Wang, Y. Jiao, X. Ouyang, S. Guo, P. Liu, H. Ao and C. Cao, *J. Lumin.*, 2019, **212**, 23–28.
- 20 L. K. Bharat, K. G. Krishna and J. S. Yu, *J. Alloys Compd.*, 2017, **699**, 756–762.
- 21 A. K. Kunti, L. Ghosh, S. K. Sharma and H. C. Swart, *J. Lumin.*, 2019, **214**, 116530.
- 22 T. Jeyakumaran, N. Venkatesh Bharathi, R. Shanmugavel, P. Sriramachandran and S. Ramaswamy, *J. Inorg. Organomet. Polym. Mater.*, 2020, **31**, 695–703.
- 23 S. Ekambaram, K. C. Patil and M. Maaza, *J. Alloys Compd.*, 2005, **393**, 81–92.
- 24 S. S. Pitale, M. Gohain, I. M. Nagpure, O. M. Ntwaeaborwa, B. C. B. Bezuidenhout and H. C. Swart, *Phys. B*, 2012, **407**, 1485–1488.
- 25 P. Sharma, P. Singh and Kamni, *Phys. B*, 2021, **602**, 412500.
- 26 N. Zhang, J. Li, J. Wang, R. Shi, L. Chen, A. Zhang and P. Yang, *RSC Adv.*, 2019, **9**, 30045–30051.
- 27 H. Chen, J. Zhou, H. Zhang and Z. Hu, *Opt. Mater.*, 2019, **89**, 132–137.
- 28 Y. Lv, K. Liu, J.-W. Shi, Z. Li, J. Li, X. Ji, D. Ma, Y. Zou, Y. Cheng and C. Niu, *J. Lumin.*, 2021, **234**, 117948.
- 29 H. Zhou, N. Guo, Q. Liang, Y. Ding, Y. Pan, Y. Song, R. Ouyang, Y. Miao and B. Shao, *Ceram. Int.*, 2019, **45**, 16651–16657.
- 30 X. Zhang, Z. Zhu, Z. Sun, Z. Guo and J. Zhang, *J. Lumin.*, 2018, **203**, 735–740.
- 31 N. Z. Khan, S. A. Khan, L. Zhan, A. Jalil, J. Ahmed, M. A. M. Khan, M. T. Abbas, F. Wang and X. Xu, *J. Alloys Compd.*, 2021, **868**, 159257.
- 32 P. Dang, G. Li, X. Yun, Q. Zhang, D. Liu, H. Lian, M. Shang and J. Lin, *Light: Sci. Appl.*, 2021, **10**, 29.
- 33 P. Du and J. S. Yu, *Chem. Eng. J.*, 2017, **327**, 109–119.
- 34 J. Zhou, X. Huang, J. You, B. Wang, H. Chen and Q. Wu, *Ceram. Int.*, 2019, **45**, 13832–13837.
- 35 P. Du and J. S. Yu, *Dyes Pigm.*, 2017, **147**, 16–23.
- 36 P. Srilakshmi, A. U. Maheswari, V. Sajeev and M. Sivakumar, *Mater. Today: Proc.*, 2019, **18**, 1375–1379.
- 37 X. Huo, Z. Wang, C. Tao, N. Zhang, D. Wang, J. Zhao, Z. Yang and P. Li, *J. Alloys Compd.*, 2022, **902**, 163823.
- 38 Z. Lei, S. Jiang, X. Wang, Y. Li, Y. Wang, J. Xie, F. Ling, Y. Wang, G. Xiang, L. Li and X. Zhou, *Ceram. Int.*, 2022, **48**, 30005–30011.
- 39 J. Fu, L. Zhou, Y. Chen, J. Lin, R. Ye, D. Deng, L. Chen and S. Xu, *J. Alloys Compd.*, 2022, **897**, 163034.
- 40 L. Zhou, W. Wang, D. Xu, Z. Wang, Z. Yi, M. Wang and Z. Lu, *Ceram. Int.*, 2021, **47**, 34820–34827.
- 41 C. Wang, Y. Jin, R. Zhang, Q. Yao and Y. Hu, *J. Alloys Compd.*, 2022, **894**, 162494.
- 42 Y.-C. Lin, M. Bettinelli and M. Karlsson, *Chem. Mater.*, 2019, **31**, 3851–3862.
- 43 H. Guo, B. Devakumar, R. Vijayakumar, P. Du and X. Huang, *RSC Adv.*, 2018, **8**, 33403–33413.
- 44 F. Liu, D. Deng, M. Wu, B. Chen, L. Zhou and S. Xu, *J. Rare Earths*, 2021, **39**, 261–268.

